Harmonic Imaging of Stem Cells in Whole Blood at GHz Pixel Rate

Karpf, Sebastian; Glöckner Burmeister, Nina; Dubreil, Laurence; Ghosh, Shayantani; Hollandi, Reka; Pichon, Julien; Leroux, Isabelle; Henkel, Alessandra; Lutz, Valerie; Jurkevičius, Jonas; Latshaw, Alexandra Lane; Kilin, Vasyl; Kutscher, Tonio; Wiggert, Moritz [**and 6 more**]

How to cite

KARPF, Sebastian et al. Harmonic Imaging of Stem Cells in Whole Blood at GHz Pixel Rate. In: Small, 2024, p. 2401472. doi: 10.1002/smll.202401472

This publication URL: https://archive-ouverte.unige.ch/unige:177767

Publication DOI: 10.1002/smll.202401472

NANO · MICRO small
www.small-journal.com

Harmonic Imaging of Stem Cells in Whole Blood at GHz Pixel Rate

Sebastian Karpf, Nina Glöckner Burmeister, Laurence Dubreil, Shayantani Ghosh, Reka Hollandi, Julien Pichon, Isabelle Leroux, Alessandra Henkel, Valerie Lutz, Jonas Jurkevičius, Alexandra Latshaw, Vasyl Kilin, Tonio Kutscher, Moritz Wiggert, Oscar Saavedra-Villanueva, Alfred Vogel, Robert A. Huber, Peter Horvath, Karl Rouger, and Luigi Bonacina*

The pre-clinical validation of cell therapies requires monitoring the biodistribution of transplanted cells in tissues of host organisms. Real-time detection of these cells in the circulatory system and identification of their aggregation state is a crucial piece of information, but necessitates deep penetration and fast imaging with high selectivity, subcellular resolution, and high throughput. In this study, multiphoton-based in-flow detection of human stem cells in whole, unfiltered blood is demonstrated in a microfluidic channel. The approach relies on a multiphoton microscope with diffractive scanning in the direction perpendicular to the flow via a rapidly wavelength-swept laser. Stem cells are labeled with metal oxide harmonic nanoparticles. Thanks to their strong and quasi-instantaneous second harmonic generation (SHG), an imaging rate in excess of 10 000 frames per second is achieved with pixel dwell times of 1 ns, a duration shorter than typical fluorescence lifetimes yet compatible with SHG. Through automated cell identification and segmentation, morphological features of each individual detected event are extracted and cell aggregates are distinguished from isolated cells. This combination of high-speed multiphoton microscopy and high-sensitivity SHG nanoparticle labeling in turbid media promises the detection of rare cells in the bloodstream for assessing novel cell-based therapies.

1. Introduction

In recent years, preclinical studies in the field of regenerative medicine have brought forth new treatment prospects for a number of pathologies, including muscle diseases such as muscular dystrophies, cardiovascular diseases, and bone injuries.[1] This has stimulated researchers to investigate new techniques for multi-scale examinations of transplanted cells, including their ability to exit the bloodstream, tendency to form aggregates in systemic circulation, and accumulation in filter organs (lung, liver, and kidney) over time.[2,3] In this context, multiphoton microscopy represents an enabling tool thanks to the possibility to acquire 3D images (including in vivo) with penetration depths substantially larger than linear optical techniques at sub-micron resolution.[4–6] So far, fluorescence-based reporters have represented the main avenue in most of bio-imaging protocols thanks to their brightness,

S. Karpf, N. Glöckner Burmeister, A. Henkel, V. Lutz, J. Jurkevičius, T. Kutscher, A. Vogel, R. A. Huber
Institute of Biomedical Optics (BMO)
University Of Luebeck
23562 Luebeck, Germany
E-mail: sebastian.karpf@uni-luebeck.de

L. Dubreil, J. Pichon, I. Leroux, O. Saavedra-Villanueva, K. Rouger
Oniris, INRAE, PAnther
Nantes F-44307, France

S. Ghosh, A. Latshaw, V. Kilin, M. Wiggert, L. Bonacina
Department of Applied Physics
Université de Genève
Rue de l'Ecole-de-Médecine, 20, Geneva 1205, Switzerland

R. Hollandi, P. Horvath
Synthetic and Systems Biology Unit
Biological Research Centre (BRC)
Szeged H-6726, Hungary

The ORCID identification number(s) for the author(s) of this article can be found under https://doi.org/10.1002/smll.202401472

DOI: 10.1002/smll.202401472

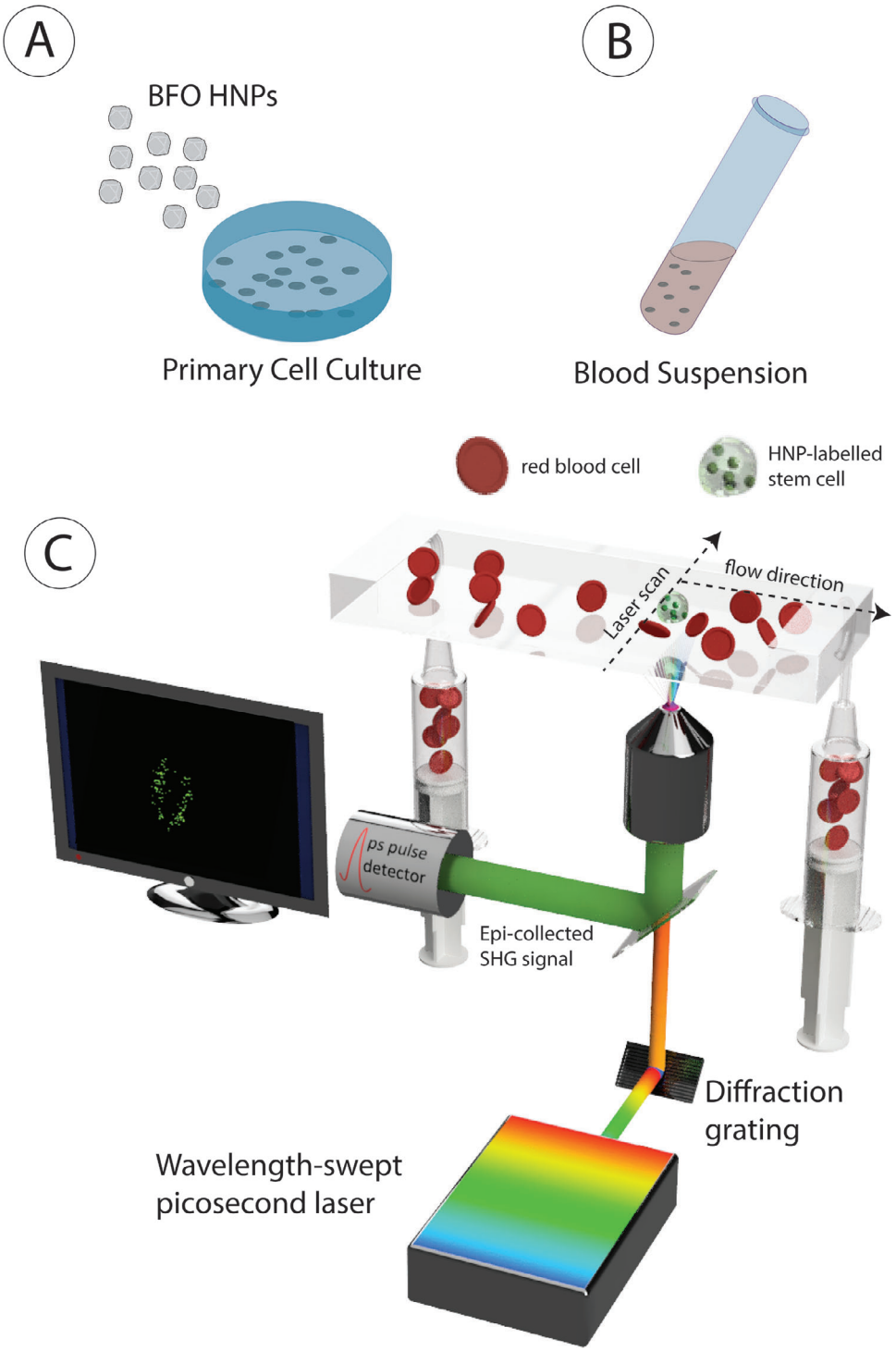

Figure 1. A) Adult stem cells isolated from skeletal muscles are directly labeled by HNPs and successively B) suspended in whole blood. C) The blood sample is circulated in a 100 × 200 μm^2 fluidic channel. The output of a continuously wavelength-swept picosecond laser is scanned orthogonally to the stream after being diffracted off a grating. The cells are illuminated in turbid media and the epi-collected SHG signal is used to acquire a continuous image of the labeled cells present in the blood flow.

molecular selectivity, access to multiplexing, and the possibility of being genetically encoded.

Interestingly, multiphoton microscopy also grants access to nonlinear parametric response[7] and offers the possibility to generate signals beyond fluorescence, such as second and third harmonic generation (SHG, THG), and multiple frequency mixings.[8–12] Such imaging modalities provide distinct advantages: they are less prone to bleaching than fluorescence, they are not associated with molecular energy levels thus allowing flexible excitation/detection wavelengths for deeper penetration, and their emission is spectrally narrower. With the recent availability of compact light sources based on optical parametric oscillators (OPO) or amplifiers (OPA),[13] properties of nonlinear parametric signals can now be utilized in the short-wave infrared (SWIR) spectral range, leading to increased penetration depth[14,15] and mitigating autofluorescence. Importantly, the quasi-instantaneous response of parametric signals, so far rarely exploited, is compatible with extreme imaging speed characterized by dwell times approaching or shorter than typical fluorescence lifetimes (nanoseconds). These speeds are not accessible by resonant scanners but recently introduced spectro-temporal encoded multiphoton microscopes (known as SLIDE microscopes) can successfully achieve MHz line-scan rates and GHz pixel rates (or, equivalently, nanosecond dwell times).[16] Here the fast-axis line scanning is achieved by optical diffraction of a rapidly wavelength-swept laser.[16] Such scanning speed requires sizeable signal levels with lifetimes shorter than a nanosecond to yield high-speed, high-sensitivity detection. Metal oxide harmonic nanoparticles (HNPs) represent a thoughtful choice as imaging probes because SHG originates from the bulk rather than from the particle's surface[17] leading to a large conversion efficiency for selected materials as reported in multiple publications by ours and other research groups.[18–26]

In this work, we center our investigation on tools for monitoring a cell therapy to counter Duchenne muscular dystrophy (DMD), a severe X-linked recessive neuromuscular disease leading to the progressive degeneration of skeletal and cardiac muscles.[27] Existing treatments only offer palliative relief, and patients with DMD typically die in their twenties due to respiratory muscle weakness or cardiomyopathy. Some of the authors have demonstrated that the systemic delivery of allogenic muscle-derived stem cells induces long-term muscle repair and clinical efficacy in DMD dogs.[28,29] In this context, simultaneous SHG/THG imaging was previously applied on human muscle-derived stem (hMuStem) cells[30] labeled by bismuth ferrite ($BiFeO_3$, BFO) HNPs.[31] We showed that HNP aggregates could be imaged at more than 1 mm depth in healthy skeletal muscle.[32] Here we apply the same cellular model and nanoparticles in combination with a multiphoton SLIDE microscope based on a wavelength-swept picosecond laser source centered at 1060 nm,[16] as shown in **Figure 1**. This system images at frame rates up to 16 kHz with sub-micron resolution at 1 GHz pixel rate. Below we describe in detail the SLIDE performance in comparison with a resonant-scanner, femtosecond laser multiphoton microscope. We then demonstrate the possibility to detect and characterize individual stem cells and stem cell aggregates flowing in whole blood without any prefiltration and discuss the detection efficiency. In the conclusion we consider the implications of this approach toward cell-based therapies.

Table 1. Excitation and detection settings of the multiphoton microscope coupled to a femtosecond laser source (fs-MP) and SLIDE system based on a picosecond wavelength-swept source (ps-SLIDE) used to acquire the images in Figure 2.

Parameter	fs-MP	ps-SLIDE	ps-SLIDE *vs* fs-MP
Wavelength	1040 nm	1060 nm	
Pulse Bandwidth	13.3 nm	0.06 nm	222× narrower
Pulse Duration	120 fs	30 ps	250× longer
Average Power	5 mW	700 mW	140×
Pulse Energy	62 pJ	700 pJ	11×
Peak Power	514 W	23.3 W	22× lower
Dwell Time	0.2 µs	1 ns	200× shorter
Pulse/Pixel	16	1	
Duty Cycle	10^{-5}	0.03	3000×
Pixel illumination time	1.9 ps	30 ps	16×
Pixel excitation integral ($P^2_{peak} \cdot t_{illum}$)	0.5 kW^2 ps	0.016 kW^2 ps	32× lower
Objective NA	1.1	1.4	

2. Results

2.1. Imaging Comparison between SLIDE and Femtosecond Laser-Based Multiphoton Microscopy

We first compared a traditional multiphoton microscope coupled to a femtosecond laser (fs-MP) and equipped with a hybrid scanner (15 kHz line scan rate) with a ≈200-fold faster SLIDE microscopy setup based on a wavelength-swept source with 30 ps pulse duration (ps-SLIDE). A detailed account of the excitation parameters is provided in the Experimental Section, **Table 1**. We imaged HNP-labeled hMuStem cells immobile on a substrate after assessing the labeling efficiency and ensuring that they are not negatively affected by the presence of the particles. Results of aptosis and proliferation bio-assays are reported in the Experimental Section and in Section S5 (Supporting Information). Further assessments of BFO-cells interactions are provided in previous works.[32,33] **Figure 2** shows that both approaches exhibit overall similar sensitivity performances despite differences in the field of view resulting from the different objective magnifications (25× vs 60×). The result of the comparison is notable, as ps-SLIDE operates at more than two orders of magnitude higher frame rate. In order to achieve the ≈200-fold increased imaging speed, ps-SLIDE employs a 3000-fold higher duty cycle excitation (30 ps pulses at 1 GHz repetition rate), causing a 140-times higher average excitation power and substantially lower peak power, P_{peak} (22-times lower). Comparing the ps-SLIDE approach with fs-MP, one would expect a significant decrease in nonlinear generation efficiency as the latter scales as P^2_{peak}. However, following the calculation of Denk et al.,[34] this loss is partly compensated by the longer excitation duration (30 ps vs 1.9 ps effective pixel illumination time). This scaling has been reported in the past.[35–37] To quantitatively account for the signal integration during the pulse, we define the Pixel Excitation Integral (PEI) for SHG as a figure of

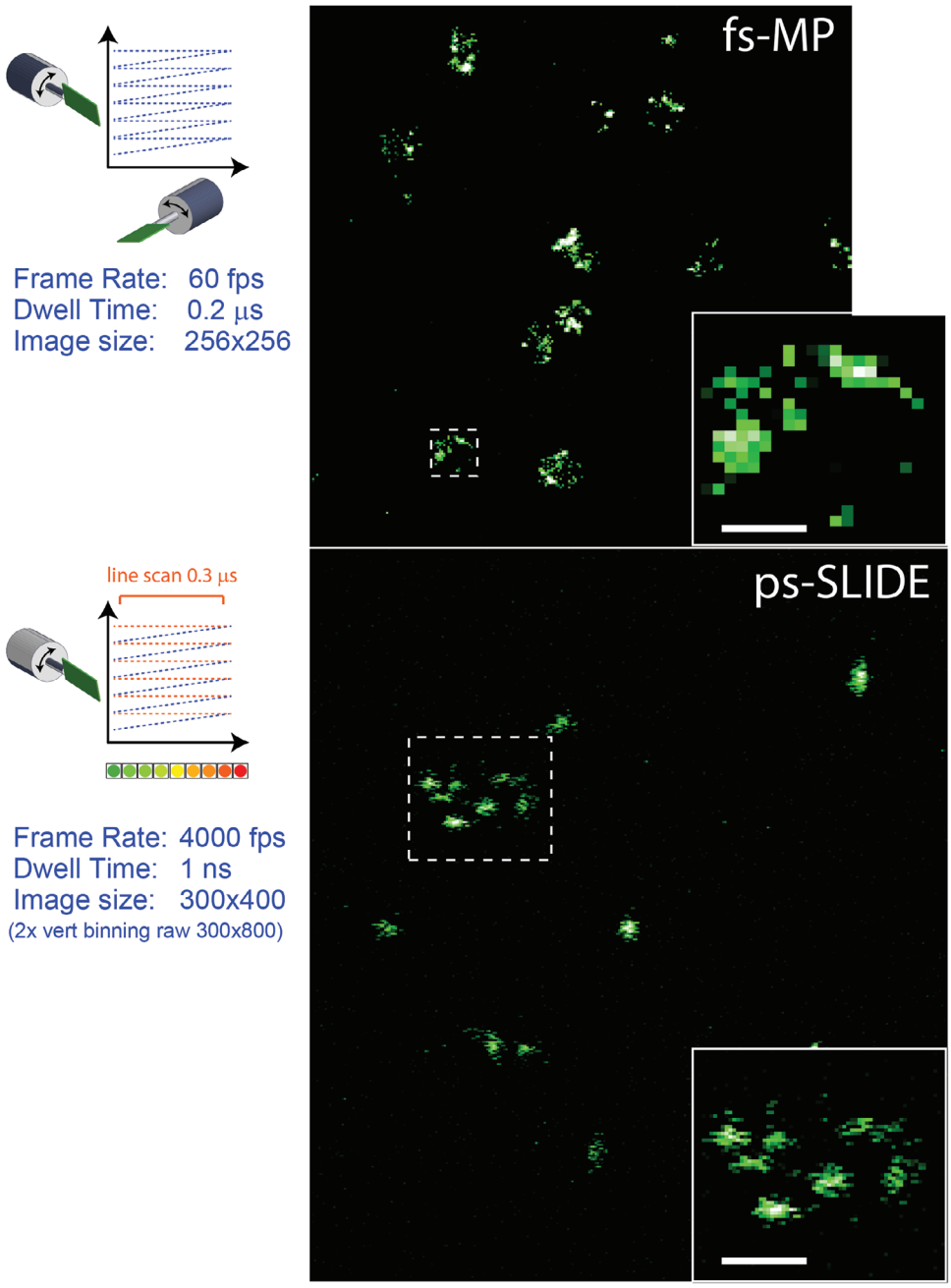

Figure 2. Fast imaging modality comparison of BFO HNP labeled hMuStem cells on a microscope substrate performed by "fs-MP" equipped with resonant-scanner (*x*, *y*) and "ps-SLIDE" operating by diffractive scanning (*x*) and galvo-mirror scanning (*y*). The dashed squares indicate the position of the ROIs magnified in the insets. Images are displayed with a logarithmic color axis and value range optimized to enhance the image contrast. Inset scale-bar: 5 µm.

merit proportional to the number of photons generated per pixel obtained as the product of P^2_{peak} and the effective illumination time (see Table 1). This way, one can show that the ps-SLIDE measurement implies a 32-times lower PEI, substantially closer to fs-MP than the almost 500-fold difference one would assume by restricting the comparison solely to P^2_{peak}. The frame rates for the images in Figure 2 are 60 fps for an image size of 256×256 pixels and 4000 fps for 300×800 pixels (binned to 300×400, see Experimental Section) for fs-MP and ps-SLIDE, respectively. The 67-fold increase is limited by the speed of the galvo scanner in the slow axis. In terms of line-scan rate and dwell times, SLIDE reaches 215 and 254 times faster rates, with dwell times as short as 1 ns (limited by the 1 GHz bandwidth of the SHG detector). The low speed of the galvo scanner leads to an elongated aspect ratio when working at 4 kHz image rate, which is corrected by vertical two times binning (Figure S2, Supporting Information).

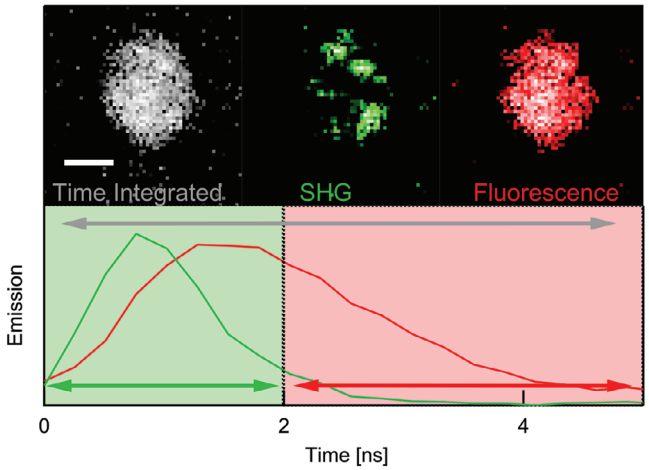

Figure 3. Time-gated acquisition. Time-resolved ps-SLIDE image of a Nile Red-stained stem cell labeled with BFO HNPs. The pixel rate was programmed to 160 MHz or 6 ns pixel dwell time. The SHG-signal was attenuated eightfold using an optical filter to yield similar signal levels to the fluorescence (Experimental Section and section S1, Supporting Information). Image acquisition time 250 µs. Scale bar 5 µm.

A key element to access these extreme imaging conditions is the use of SHG as a reporter signal. This optical process occurs quasi-instantaneously[7] as opposed to fluorescence, which is typically characterized by nanosecond lifetimes.[38] This aspect is illustrated in **Figure 3**, where we compare the temporal response of fluorescence and SHG from a hMuStem cell labeled by BFO HNPs and costained by Nile Red for morphological contrast. The left image integrated over the full temporal span (grey arrow) shows the whole object shape. Gating the signal emitted during the first 2 ns after pulse excitation (green) preferentially reveals the SHG emitted by BFO HNPs. The signal gated between 2 and 6 ns (red) is associated with fluorescence. Note that here we programmed a pulse repetition of 160 MHz and 814 kHz line scan rate to accommodate the fluorescence decay time (details in section Section S1, Supporting Information).[16] This corresponds to a pixel dwell time of ≈6 ns. To lower the stronger SHG signal to the fluorescence level, we attenuated the SHG signal by a spectral long-pass filter (Experimental Section).

2.2. SLIDE Cell Counting and Sizing in Blood

For high-speed, high-sensitivity cell detection in turbid media, we employed the ps-SLIDE system to detect labeled cells suspended in blood and analyze the morphology to detect aggregates. According to the optical arrangement sketched in Figure 1c, one imaging axis is scanned by spectro-temporal scanning while the orthogonal axis is scanned by the flow. The line scan covers a field of view of 67 µm, sampled with 300 pulses (3.3 MHz line scan rate, 1 GHz pixel rate). From the sampled time trace, images were generated with an image size of 300 × 200 pixels, corresponding to 16 kHz frame rate (62.5 µs per image).

For hMuStem cell detection experiments, cells were suspended at $C_{cell} = 4 \times 10^5$ cells mL^{-1} concentration in whole human blood. The ratio of target cells (hMuStem) to red blood cells in our experiment approximately amounts to 4 in 10^5, assuming the presence of $\approx 9 \times 10^9$ erythrocytes mL^{-1}. The sample was circulated through a microfluidic chamber of 200 × 100 µm^2 cross section at 10 µL s^{-1} volume rate. For intensity-based cell detection, a threshold was established to separate cell detections from electronic noise. For this, the dark count rate was determined as (1.9 ± 1.5) pixels counts in a 300 × 400 px region of the continuous image stream. Assuming a Poissonian intensity distribution, we defined the threshold for cell detection conservatively by an intensity six times the standard deviation (6σ) over the mean, corresponding to a false-positive rate of <4 per million. The 300 × 400 px regions of the image stream used for sensing and imaging (see Figure S4, Supporting Information) hence only include images with at least 11 nonzero pixels (i.e., pixels with photons). On the left side of **Figure 4**, we present the nonzero pixel histograms associated with dark noise regions (top plot) and images with above-threshold photon detections (bottom plot). On the right side, we provide some examples of the latter class. A subset of these images (215) were annotated by a human operator and used as a training set for artificial intelligence-based cell analysis.

2.3. Automated Cell Detection

To automate the quantification of cell detection events and extract morphological information, we applied a deep learning instance segmentation model ("nucleAIzer").[39] After obtaining the segmentation masks from "nucleAIzer", we applied post-processing techniques to address overlapping detections. Our system successfully differentiated between labeled cells and sparse pixel events associated with detector dark noise and cosmic rays by taking into account the average pixel intensity and spatial distribution relative to typical cell sizes. **Figure 5** illustrates these categories; the red outlines indicate single-pixel events, while the green outlines are the result of the automatic segmentation of objects recognized by "nucleAIzer" as events to retain. We further refined our analysis by subjecting segmented objects larger than single-pixel events to additional scrutiny. Specifically, we evaluated these objects based on predefined thresholds for average intensity and the sum of intensities within their detected shapes. Objects falling below the threshold values were excluded from the analysis (red crosses in Figure 5), while those surpassing the thresholds were reclassified, denoting their increased significance and relevance.

This approach was applied to a continuous high-speed image stream of flow corresponding to V_{tot} = 94.5 µl of whole blood resulting in 2.55 × 10^3 cell counts and 89.75 × 10^3 single pixel events acquired in 9.45 s. The measurement time was limited by the storage capacity of the acquisition system. The detection yield of hMuStem cells can be estimated by comparing these figures to the theoretically expected number of detections, obtained by multiplying the hMuStem cell concentration by the overall volume of the sample that was circulated throughout the experiment: $C_{cell} \times V_{tot} = 3.78 \times 10^4$ cells. This value needs to be rectified by considering the partial spatial overlap (6.7%) of the imaging region with the channel section (see. Section S3, Supporting Information). An additional correction stems from the flow velocity profile within the flow chamber, leading to a flow speed (and therefore probed volume) in the central region two times larger than the average flow rate (see Experimental Section).[40] Overall, this

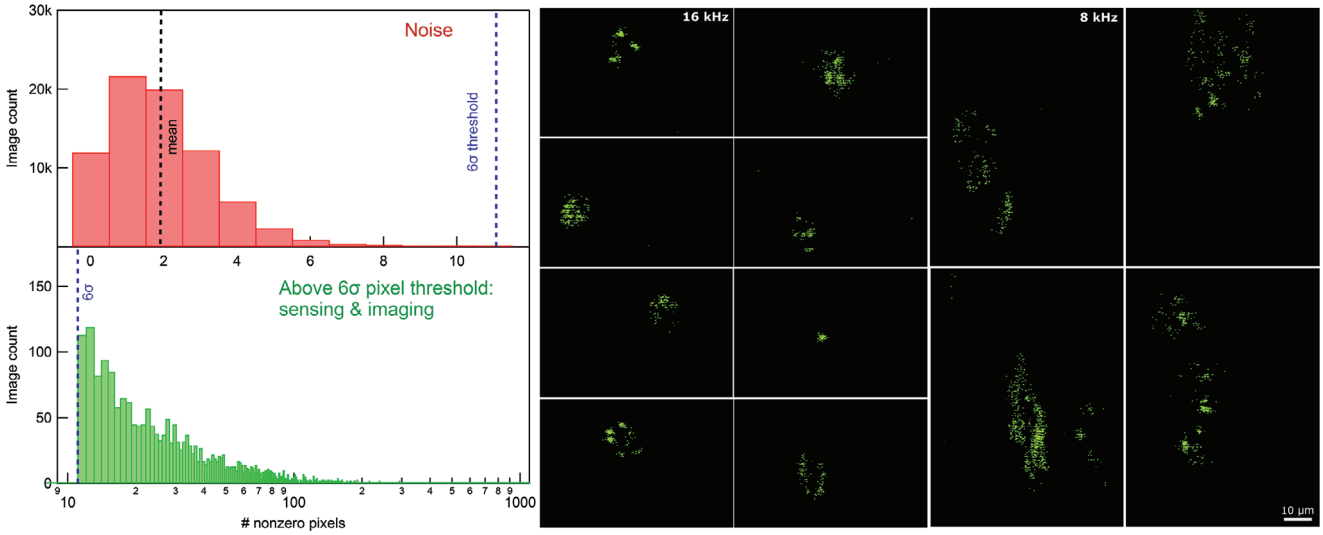

Figure 4. SLIDE flow imaging cell detection in whole blood. Left: Noise histogram (upper plot) with overlayed mean+6σ intensity-based threshold for sensing. Any 300 × 400 px image with more than 11 nonzero pixels represents a detection event (lower plot, note the log scale). Right: SHG in flow images acquired at 16 kHz (300 × 200 px, left images) and 8 kHz frame rate (300×400 px, right images). Scale bar 10 µm.

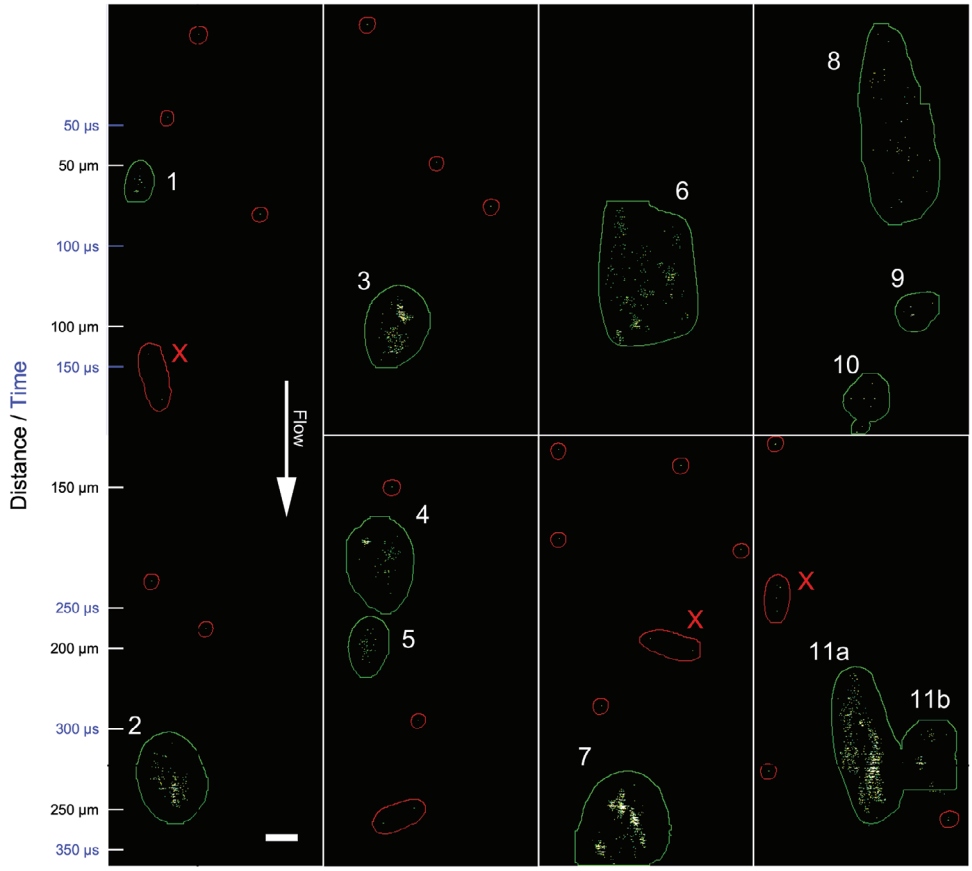

Figure 5. In-flow detections and segmentation. Exemplary images of automatic cell detections in whole blood. The vertical axis displays the temporal delay from the top of the image and the corresponding distance calculated from the flow speed (see Experimental Section). The SHG in cells appears as green spots. The automatic detection algorithm allows distinguishing isolated pixels associated with dark noise (red outlines) from cell-like objects retained for the morphological analysis (green outlines). The object labels are also used in the scatter plot of Figure 6. Some sparsely labeled objects were discarded based on validation criteria relying on average intensity thresholds (red crosses). Scale bar 10 µm.

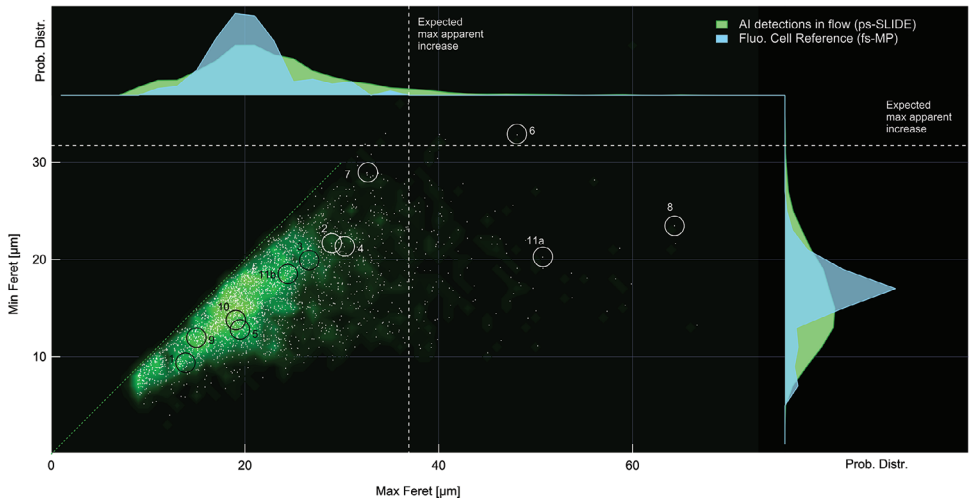

Figure 6. Summary of detections. The scatter plot displays the maximum and minimum Feret's diameter determined by the "nucleAIzer" analysis of in-flow detections (white dots) superposed to the corresponding heat-map (green). Along the green diagonal line, the two Feret's diameters are identical. The circles mark the detections corresponding to the in-flow images of Figure 5. Comparison with the morphology of fluorescent cells in suspension. Probability distributions of the length of the maximum (top panel) and minimum (right panel) Feret's diameter established for a suspension of fluorescence labeled cells (blue curves) and HNP-labeled cells detected by SLIDE in flowing blood and successively segmented by "nucleAIzer" (green curves). The vertical and horizontal dashed white lines correspond to the expected apparent size of a cell with min and max Feret's diameters at the maximum of the fluorescence reference distribution when detected at ±10 µm from the focal plane (Figure S5, Supporting Information).

would result in a theoretical number of $\approx 5\times 10^3$ target cells flowing through the "imaging region" during measurement. Taking these two corrections into account and assuming the spatially homogeneous distribution of cells in flow, SLIDE flow imaging is able to detect ≈ 50% of the target cells at a throughput rate of 536 target cells per second. Interestingly, the high sensitivity of the system leads to a large vertical "sensing region". Thus, we can ascribe some of the discarded detections (a few sparse pixels in a large area, denoted by red crosses in Figure 5) to strongly out-of-focus cells. This effect can be appreciated by inspecting the data treatment and images in Figures S5 and S6 (Supporting Information). We expect that both throughput and detection yield can be increased by the use of special optics to generate an elongated focus (e.g., Bessel beam). Already now, we can positively rule out false positive events in our approach, due to the extremely low background, the high SHG signal levels, and the strict rejection criteria applied.

All detections meeting the validation criteria (e.g., green outlines in Figure 5) were successively analyzed for extracting essential morphological parameters. In the main panel of **Figure 6**, the white dots indicate the Max/Min Feret's diameter pair of individual detections (a different representation of the same dataset including some additional outliers is reported in Figure S6, Supporting Information). The heatmap in green visualizes the density of the corresponding distribution for easier inspection. The detections labeled 1–11 correspond to the green shapes in Figure 5. In the top and right insets of Figure 6, we separately report the distribution of the Max and Min Feret's diameters (green curves) superposed to the same parameters measured on a set of 163 fluorescence-labeled cells in suspension on the fs-MP reference system (blue curves, Section S2, Supporting Information). The latter are considered as reference measurements, as the fluorescence labeling reveals the entire cell morphology at the cost of lower signal and lower speed. The curves for Min and Max Feret's diameter are well overlapped, with the maxima of the probability distributions occurring approximately at the same values. The distributions of HNP-labeled cells in blood are slightly broader, consistent with the results of a measurement relying on the highly inhomogeneous arrangement of HNPs within cells for morphology reconstruction. The asymmetry toward longer values of the green distributions arises because out-of-focus detections are associated with apparently larger dimensions (dashed white lines in Figure 6; discussion in Section S3, Supporting Information).

Taking into account all of these elements, we attribute the events labeled 1–5 to detections of isolated cells with sizes within the main peak of the reference distribution (blue). Interestingly, the tail of the Max Feret's diameter distribution (green curve) extends toward much larger sizes (i.e., 60–80 µm: up to three/four times the maximum of the distribution and clearly larger than the upper estimation for defocused detection of a single cell). We identify these larger objects as cell aggregates, which is supported by the images labeled 6–11 in Figure 5. Thus, based on the multiparametric output of SLIDE flow-imaging, we can assign average and maximum intensity to these detections, as reported in Figure S5 (Supporting Information). This allows us to better refine their assignments as aggregates and distinguish them from strongly out-of-focus cells in ambiguous situations.

3. Discussion and Conclusion

In this work, we demonstrate the image-based detection of flowing hMuStem cells and cell aggregates in turbid media. The system showed a detection efficiency of 50%, enabling high throughput imaging cell detection at 530 cells s^{-1}. The high-sensitivity, background-free harmonic imaging of nanoparticle-labeled cells embedded in whole blood paves the way toward in vivo blood flow imaging.

For prospective clinical adoption, screening procedures should inform about the presence of cells in the systemic circulation and address concerns related to the risks induced by stem cell infusion and aggregation into cellular clumps that can lead to major adverse vascular effects. Cell aggregates can also increase thrombogenic risk[41,42] as it has been shown that mesenchymal stem cells (MSCs) express procoagulant activity linked to the expression of tissue factor that, when in contact with blood, initiates coagulation.[43] Gleeson et al.[44] found that intra-coronary infusion of bone marrow-MSCs in a porcine myocardial infarction model was associated with a mortality rate of 60% attributed to exacerbated microvascular obstruction due to platelet-rich thrombi containing infused cells. In transplanted patients, thrombogenic events have also been described during infusions of stem cells in the context of metabolic deficiency,[45] kidney disease,[46] and chronic pancreatitis.[47]

The extremely limited number of target cells expected in the flow demands the ability to monitor large volumes of blood at high throughput to obtain statistically significant results and to be able to monitor the evolution of the therapeutic protocol over time. Similarly, the possibility to work in whole, untreated blood would prevent the risk of losing target cells during filtration and accelerate the procedure, prospectively enabling monitoring extracorporeal circulation. Whole blood displays broad autofluorescence throughout the UV–vis[48] that can hinder the signal of fluorescent reporters leading to false positive and negative detections, with a substantial decrease in sensitivity and accuracy. The use of nanoparticles (NPs) for cell labeling represents an appealing alternative, and indeed it is a research avenue already explored for imaging and tracking stem cells in preclinical models.[49–51] Unlike other settings (e.g., tracking of metastatic cells), regenerative medicine protocols allow labeling directly the cells before their administration. This possibility represents a great advantage as it lightens the burden of implementing NP surface coating strategies to increase target selectivity. The NP approach has been successfully demonstrated in combination with MRI,[49] CT, PET, fluorescence, and photoacoustic imaging,[50] for NPs of various nature (Au, QDs, UCNPs, etc.).[51] Among these imaging techniques, optical microscopy has the advantage of (sub-)cellular resolution, which is necessary for elucidating the aggregation state of flowing cells and represents a core asset for the complementary investigation of the migration and grafting of stem cells in tissues. However, purely optical approaches show comparatively poor penetration imaging depth in the host organism. The use of multi-modal nanoparticles[52–54] including HNPs[55] could mitigate the discrepancy between optically-based techniques and those operating on magnetic, radioactive, or acoustic stimuli and allow connecting different spatial-scales to address more comprehensively the challenges associated with systemic delivery of transplanted cells.

Taking these requirements into account, we have devised an approach for in-flow counting and sizing of stem cells labeled by HNPs in whole, unfiltered blood. We showed how the wavelength flexibility, the practically instantaneous response of SHG and the high signal levels enable in-flow imaging in blood, leading to the acquisition of background-free signal at high imaging rates. The scanning speed reached is too fast for the response of fluorophores but not for nonlinear parametric signals such as SHG. The imaging rate demonstrated enables screening the enteric blood volume of a mouse (2.5 mL, corresponding to 6–8% of its body weight)[56,57] in 30 min (considering 1 m s^{-1} flow speed), with the possibility to decrease even further this time by a tailored adaptation of flow cell and focusing optics. For a prospective translation of our approach in vivo, as one image dimension is scanned by the flow, one has to take into account different (lower) blood flow speeds and the necessity to correct for not constant flow with an independent calibration of the dynamics of the vessel under observation.[58,59]

We established an AI-based segmentation and analysis of detections which showed agreement with the morphological features characterized by traditional multiphoton microscopy on fluorescence labeled stem cells in suspension. Although the sparse labeling by HNPs does not grant access to fine details of cell morphology, the maximum and minimum Feret's diameters can be related in a straightforward manner to the size of flowing cells and to their aggregation state. The results were obtained based on a cell therapy protocol proposed to counter the effects of DMD as a benchmark. This suggests that the combination of SLIDE detection of SHG-emitting adult stem cells in the blood and their simultaneous SHG/THG imaging by conventional multiphoton microscopy in tissues for increased selectivity,[32] defines a comprehensive and promising approach for preclinical safety and efficacy assessments.

4. Experimental Section

Isolation and Culture of Human MuStem Cells: Biopsies were collected from the *Paravertebralis* muscles of patients aged 12–19 years. Patients were free of known muscle disease and operated for acute scoliosis at the Department of Pediatric Surgery of the "Centre Hospitalier Universitaire" (CHU) de Nantes (France). All patients gave written informed consent. All protocols were approved by the Clinical Research Department of the CHU (Nantes, France), according to the rules of the French Regulatory Health Authorities (approval number: MESR/DC-2010-1199). The biological sample bank was created in compliance with national guidelines regarding the use of human tissue for research (approval number: CPP/29/10).

Human MuStem cells (hMuStem cells) were independently isolated from skeletal muscle from four patients after 6 days using a modified version of the preplating technique as previously described.[30,60] Cells were seeded on CELLstart substrate-coated plastic flasks (Invitrogen, Cergy-Pontoise, France) at 5.0×10^4 cells cm^{-2} under standard conditions (37 °C in 95% humidified atmosphere containing 5% CO_2) and expanded in growth medium (Macopharma, Mouvaux, France), supplemented with 10% human serum (EFS, Nantes, France), 1% 10000 IU mL^{-1} penicillin, 10 mg mL^{-1} streptomycin, 25 mg mL^{-1} fungizone (PSF; Sigma–Aldrich, Saint–Quentin–Fallavier, France), 10 ng mL^{-1} human recombinant basic fibroblast growth factor (bFGF; Miltenyi, Bergisch Gladbach, Germany), and 25 ng mL^{-1} human recombinant epidermal growth factor (EGF; Miltenyi). Growth medium was replaced every 3 days.

Human MuStem Cells Labeling by BFO HNPs: Human MuStem cells ($n = 4$, independent batch) were expanded in growth medium for 8 hours at 37 °C to generate up to 1.125×10^6 cells in a T75 plastic flask (Corning, NY, USA) and 1.95×10^5 cells in the Ibidi-8 well chamber (IBIDI, Gräfelfing, Germany). For this study, uncoated BFO-HNPs previously synthesized according to the protocol detailed in Schwung et al.[31] were used. The particles were received and suspended in solution at 5 mg mL^{-1} in 100% ethanol. These HNPs were the same used and characterized in other studies.[32,61] Cells were exposed to previously sonicated BFO HNPs at 75 µg mL^{-1} concentration. After 18 hours, culture medium was removed in

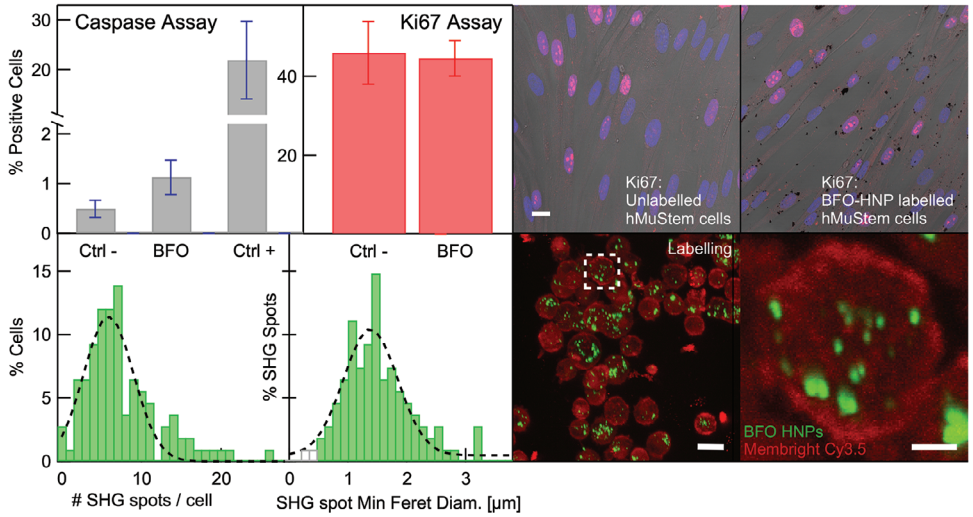

Figure 7. Toxicity profile and labeling efficiency of BFO HNPs on hMuStem cells. First row; "Caspase Assay" Results for staurosporine-treated hMuStem cells (Ctrl+), unlabeled hMuStem cells (Ctrl-), and BFO HNPs-labeled hMuStem cells (BFO). Note the split in the vertical axis. "Ki67 Assay" Results for untreated hMuStem cells (*Ctrl-*) and BFO HNPs-labeled hMuStem cells (*BFO*) and corresponding microscopy images (red: Alexa 555 fluorescence associated with Ki67; blue: DAPI for nuclear staining; gray: overlay of the bright-field image with BFO HNP aggregates appear as dark spots). Scale-bar 20 µm. Second row; Cell labeling efficiency was analyzed using maximum intensity projection images as the one reported in the two rightmost panels (red: Membright Cy3.5 fluorescence; green: SHG by BFO HNP aggregates). Scale-bar 20 µm. The ROI in the dashed outline is magnified in the bottom-right panel. Scale-bar 5 µm. The histograms in the left panels report the distribution of the number of SHG spots per labeled cell and their minimal Feret's diameter fitted by Gaussian functions (dashed lines).

order to eliminate the excess of BFO HNPs and primary cell cultures were maintained for 3 days at 37 °C. Cells expanded in T75 plastic flask were then trypsinized (Fisher scientific, Waltham, MA, USA), counted, and suspended at 10^5 cells mL^{-1} in phosphate buffered saline (PBS) containing 8% PFA to obtain fixed labeled cells without presence of aggregates. Cell suspension was centrifuged and the pellet was taken up in PBS. For specific measurements, BFO HNP-labeled cells (10^6 cell mL^{-1}) were stained with MemBright-Cy3.5 (200 nM, Idylle, Paris, France).

Assessment of Toxicity and Labeling Efficiency of BFO HNPs: In **Figure 7**, the results of Caspase and Ki67 assays to quantify cell apoptosis and proliferation, respectively. By the Caspase assay, it was determined that the percentage of positive cells was 1.12% ± 0.35% and 0.49% ± 0.17% for labeled (*BFO*) and untreated hMuStem cells (Ctrl-), respectively, indicating low induction of apoptosis following nanoparticle uptake (see details in Section S5, Supporting Information).

Similarly, the results obtained with the canonical proliferation marker Ki67 on labeled (BFO) and unlabeled (Ctrl-) hMuStem cells indicate that the proportion of cycling cells are not statistically different. This finding showed that the proliferation activity of hMuStem cells was not undermined by the presence of BFO HNPs, as demonstrated by the presence of dispersed Ki67+ cells in the brightfield image overlayed to the fluorescence image of both primary cultures. Altogether, these results confirmed those previously obtained for the same nanomaterial on various human carcinoma cell lines[33] and those recently established for hMuStem cells at lower BFO HNP concentrations (12.5 and 25 µg mL^{-1}).[32]

The labeling efficiency was extracted and quantified from a series of images similar to the one reported in the bottom right panel of Figure 7. The image was obtained as a maximum intensity projection of a stack of 41 slices acquired with 0.375 µm step size. From the analysis performed on one hundred cells, the distributions of SHG spots per cell were computed, and their minimum Feret's diameter as reported in the histograms in the second row. The two distributions were fitted by Gaussian functions peaking at 5.9 SHG spots $cell^{-1}$ and 1.4 µm, respectively. These values could be readily compared with the close-range image of a cell in the rightmost plot, corresponding to the ROI defined by the white dashed outline in the "Labeling" plot. Generally, a rather sparse labeling of cells was found by BFO HNP aggregates. This was consistent with the previous observations of active nanoparticle uptake by cells and their localization in cytoplasmic vesicles mainly corresponding to endosomes for an extended time period (up to two weeks in proliferating cell culture conditions).[32]

Blood Preparation: The blood was collected from the transfusion center of the Universitätsklinikum Schleswig–Holstein (UKSH) Lübeck in EDTA tubes. All microfluidic chips and tubings were washed with Ha 1:500 Heparin:PBS solution to prevent clogging.

Imaging: fs-MP: Standard multiphoton microscopy measurements were performed at the APEX platform of the INRAE/Oniris UMR 703 PAnTher, Center of Excellence Nikon Nantes (Nantes, France) using a commercial system (A1R-MP, Nikon, Europe BV) coupled with an InSight DeepSee laser (Spectra-Physics, Irvine, CA, USA), tunable in the 680–1300 nm range, <120 fs pulses. An auxiliary beam at 1040 nm was used in combination with the tunable output for dual wavelength excitation. An apochromat 25× MP1300 immersion objective (NA 1.10, WD 2.0 mm) was employed. For the fast imaging comparison with SLIDE (Figure 2), the resonant scanning mode was used (60 fps, 256 × 256), while other images (Figure 7) were recorded using the system's galvanometric scanner. Quantification of BFO spot number and minimal axis length was performed using the GA3 module of NIS software (Nikon Instruments).

Imaging: ps-SLIDE: The SLIDE setup employed a newly built FDML laser[62] at 1060 nm center wavelength and 3.3 MHz sweep rate by employing eight times buffering.[63] A sweep span of 12 nm was employed, leading to a horizontal field-of-view (FOV) of 67 µm in combination with a 60 ×, NA 1.4 oil immersion objective. The vertical axis was scanned with a galvanometric mirror (Scanlab Dynaxis 421) driven by a 2 kHz sinusoidal waveform, leading to a bi-directional frame-rate of 4 kHz and 800 lines per frame. For correct aspect ratios, the lines were two times binned to yield images of 300×400 pixels (Figure S2, Supporting Information). For flow measurements, the galvo motion was stopped and the vertical axis scanning was performed through the flow (no vertical binning). The horizontal sampling was programmed using a custom digital waveform loaded on a 10 GS s^{-1} arbitrary waveform generator (Tektronix AWG7102), producing 300 pulses per sweep at Gigapixel s^{-1} rate. The data acquisition was driven synchronously to the SLIDE excitation pulses using a phase locked loop (PLL) to run the sample clock of the 4GS s^{-1} digitizer card

(Alazartech ATS9373) at precisely four times the pixel rate. For reference, for the sample volume probed in the main experiment described, at 6.8 GBytes s^{-1}, a total of 64 GByte of data needed to be recorded into the RAM of the computer. In the detection path, the photocurrent produced by a hybrid photomultiplier (Hamamatsu R11322U-40) was amplified by a transimpedance amplifier with 400 MHz bandwidth, which was the highest DC-coupled bandwidth available. For the equalization of the strong SHG signal and the approximately tenfold weaker fluorescence signal in 3, a cinematic color filter (LEE Filters, 025 sunset red) was used for equalization of the signal levels ($T_{635}/T_{532} = 8$). The rest of the setup was as previously described.[16]

Imaging: ps-SLIDE flow imaging set-up: The cell-blood mixture was sent through a flow chamber of 200 × 100 μm^2 cross-section and 18 mm length (Microfluidic ChipShop Germany, 10000196) using a syringe pump (Harvard Elite). To prevent sedimentation of cells, a magnetic stirrer was used inside the syringe. The flow speed in the flow chamber was empirically set to observe isotropic sampling in the *x*- (SLIDE) and *y*- (flow) direction by visualization of round-shaped cells in the SLIDE imaging flow images. In *x*-direction, the sampling is given as the ratio of the number of pixels (300) and by the field of view (FOV). The FOV is given by the objective (60×, NA 1.4 oil immersion, Nikon Apoplan 60×) and the chosen Fourier Domain Mode Locked (FDML) laser span of 12 nm. This lead to a FOV in the *x*-direction of 67 µm and a pixel pitch of 67 µm 300^{-1} px = 223 nm px^{-1}. It was noted that Nyquist sampling was achieved with 290 pixels, so a slight oversampling was programmed. In order to achieve the same sampling pitch in *y*, the movement in between line scans should match the 223 nm in *x*-direction. Considering the SLIDE line scan rate of 3.3 MHz, this translated to a flow speed of 223 nm ×3.3 MHz ≈ 0.75 m s^{-1}. This isotropic sampling was empirically achieved with a flow rate of 10 µl s^{-1} by observing fluorescent beads in flow. Alternatively, the flow velocity by the programmed flow rate on the syringe pump of 10 µl s^{-1} and the cross-sectional area of the chamber (200 ×100 μm^2) could also be calculated, leading to an average flow speed of 0.5 m s^{-1} assuming homogeneous velocity distribution within the chamber. However, by applying the theoretical framework developed by H. Bruus, a more realistic average flow velocity was evaluated within the "imaging region" of 1.025 m s^{-1}.[40] Note that this correction leads to an increase of the probed volume calculated from the nominal flow rate of the syringe, and accordingly a decrease of the calculated detection efficiency of target cells, which corresponded to the ratio between the actual number of detections and the detections expected within the probed volume. This meant that the detection efficiency ranges between 99% (no correction applied) and 50% (with correction). In a control experiment, it was verified that the irradiation conditions used in the experiment does not affect the morphology of erythrocytes by visually comparing brightfield images acquired before and after irradiation of a blood sample (1:50 dilution in a 0.6 M saline solution). It was also observed that prolonged irradiation entailing multiple raster scans over the same sample region eventually induce permanent damage on erythrocytes, therefore - if the approach is transferred in vivo - more specific assays to monitor haemolysis, and the onset of nonlinear and heat damage need to be carried out.[64–66]

Image Pre-Processing and Automated Cell Detection: The recorded raw data was pre-processed by subtracting the electronic noise (Johnson noise) of the transimpedance amplifier. A threshold of 14 mV amplitude was selected to remove all electronic noise still while still leaving any single and multi photon signals untouched (single photon levels had ≈25 mV amplitude). The thresholded data were transformed into images using the "ImageJ" Raw import option, followed by four digitization-sample-per-pixel binning. Images were then segmented to identify target cells using "nucleAIzer"[39] deep learning instance segmentation model re-trained on a training set containing 215 images out of the total of 2550 detections. The training set contained images with annotations created in the "napari-annotatorj"[67] software labeling stem cells and single-pixel spots then exported to instance-aware masks. The predicted segmentation masks were post-processed to resolve overlapping detections, and masks were separated to the 2 classes "cell/cell aggregates" (green outlines in Figure 5) and "single spots" (red outlines). Morphology and intensity features were calculated using the open source image-processing library "Scikit-Image"[68] including area, Max and Min Feret's diameters and perimeter to describe the shape, while basic statistics such as mean, standard deviation, min, max, and sum were applied to intensities under each segmented object on pre-processed images. Based on a manual selection of intensity thresholds, an additional (third) class of objects was defined for the "low-level" labeling objects containing a low number of single spots located close to each other, filtered from the cell class (red crosses in Figure 5).

Supporting Information

Supporting Information is available from the Wiley Online Library or from the author.

Acknowledgements

All research groups gratefully acknowledge the funding from the European H2020-ICT project FAIR CHARM (FAst InfraRed Coherent HARmonic Microscopy, http://www.faircharm.eu). S.K. gratefully acknowledges his Juniorprofessorship with financial support by the state of Schleswig–Holstein (Excellence chair program by the universities Kiel and Luebeck), and funding from the Deutsche Forschungsgemeinschaft (DFG, German Research Foundation) under Germany's Excellence Strategy – EXC 2167-390884018. K.R. and L.D. were partially supported by a grant from the "Fonds Européen de Développement Régional" (FEDER; N PL0003686). The authors acknowledge the support of the APEX platform of UMR703 PAnTher, Center of Excellence Nikon, member of IBiSA, NeurAtris infrastructure and Biogenouest, Nantes, France.

The authors thank PD Dr. Juhl from the transfusion center of the UKSH Lübeck for the blood samples.

Conflict of Interest

The authors declare no conflict of interest.

Author Contributions

S.K., N.G., A.H., and V.L. built and conducted laboratory experiments on the ps-SLIDE. L.D., I.L., and K.R. designed the biological procedure, prepared the samples and conducted the biotoxicity assessment. L.D. and J.P. conducted laboratory experiments on the fs-MP. V.K. performed the first feasibility assessments. J.J., M.W., and O.S.-V. conducted additional tests and control experiments on ps-SLIDE and fs-MP. R.H., and P.H. designed and conducted the automated cell segmentation. S.G., A.L., S.K., and L.B. analyzed the data. V.K., K.R, L.B., and S.K. designed the experiment and the data analysis. A.V. and R.A.H. contributed to the study and experimental setup design. S.K. and L.B. wrote the manuscript. All authors revised and approved the manuscript.

Data Availability Statement

The data that support the findings of this study are available from the corresponding author upon reasonable request.

Keywords

fiber lasers, harmonic imaging, multiphoton microscopy, nanoparticles, regenerative medicine, SHG, SLIDE

Received: February 24, 2024
Revised: May 21, 2024
Published online:

[1] A. S. Mao, D. J. Mooney, *Proc. Nat. Acad. Sci.* **2015**, *112*, 14452.
[2] A. V. Naumova, M. Modo, A. Moore, C. E. Murry, J. A. Frank, *Nat. Biotechnol.* **2014**, *32*, 804.
[3] L. Scarfe, N. Brillant, J. D. Kumar, N. Ali, A. Alrumayh, M. Amali, S. Barbellion, V. Jones, M. Niemeijer, S. Potdevin, G. Roussignol, A. Vaganov, I. Barbaric, M. Barrow, N. C. Burton, J. Connell, F. Dazzi, J. Edsbagge, N. S. French, J. Holder, C. Hutchinson, D. R. Jones, T. Kalber, C. Lovatt, M. F. Lythgoe, S. Patel, P. S. Patrick, J. Piner, J. Reinhardt, E. Ricci, et al., *NPJ Regen. Med.* **2017**, *2*, 28.
[4] W. R. Zipfel, R. M. Williams, W. W. Webb, *Nat. Biotechnol.* **2003**, *21*, 1369.
[5] K. König, *J. Microsc.* **2000**, *200*, 83.
[6] D. Kobat, M. E. Durst, N. Nishimura, A. W. Wong, C. B. Schaffer, C. Xu, *Opt. Express* **2009**, *17*, 13354.
[7] R. W. Boyd, *Nonlinear optics*, Academic Press, Cambridge **2003**.
[8] Y. Wang, C.-Y. Lin, A. Nikolaenko, V. Raghunathan, E. O. Potma, *Adv. Opt. Photonics* **2011**, *3*, 1.
[9] G. Zoriniants, F. Masia, N. Giannakopoulou, W. Langbein, P. Borri, *Phys. Rev. X* **2017**, *7*, 041022.
[10] G. Campargue, L. La Volpe, G. Giardina, G. Gaulier, F. Lucarini, I. Gautschi, R. Le Dantec, D. Staedler, D. Diviani, Y. Mugnier, J.-P. Wolf, L. Bonacina, *Nano Lett.* **2020**, *20*, 8725.
[11] P. Mahou, M. Zimmerley, K. Loulier, K. S. Matho, G. Labroille, X. Morin, W. Supatto, J. Livet, D. Débarre, E. Beaurepaire, *Nat. Methods* **2012**, *9*, 815.
[12] J. F. Ortas, P. Mahou, S. Escot, C. Stringari, N. B. David, L. Bally-Cuif, N. Dray, M. Négrerie, W. Supatto, E. Beaurepaire, *Light: Sci. Appl.* **2023**, *12*, 29.
[13] E. Herkert, N. Slesiona, M. E. Recchia, T. Deckert, M. F. Garcia-Parajo, E. M. Fantuzzi, A. Pruccoli, I. C. Ragupathy, D. Gudavičius, H. Rigneault, J. Majer, A. Zumbusch, E. Munger, S. Brasselet, A. T. Jones, P. Watson, S. A. Boppart, V. Singh, S. Borkar, F. E. Q. Rodriguez, W. Langbein, V. Petropoulos, N. F. van Hulst, M. Maiuri, G. Cerullo, D. Brida, F. Troiani, C. A. Rozzi, E. Molinari, M. Vengris, et al., *J. Opt.* **2021**, *23*, 073001.
[14] L. A. Sordillo, Y. Pu, S. Pratavieira, Y. Budansky, R. R. Alfano, *J. Biomed. Opt.* **2014**, *19*, 056004.
[15] N. Akbari, M. R. Rebec, F. Xia, C. Xu, *Biomed. Opt. Express* **2022**, *13*, 452.
[16] S. Karpf, C. T. Riche, D. Di Carlo, A. Goel, W. A. Zeiger, A. Suresh, C. Portera-Cailliau, B. Jalali, *Nat. Commun.* **2020**, *11*, 2062.
[17] L. Bonacina, P.-F. Brevet, M. Finazzi, M. Celebrano, *J. Appl. Phys.* **2020**, *127*, 230901.
[18] Y. Nakayama, P. J. Pauzauskie, A. Radenovic, R. M. Onorato, R. J. Saykally, J. Liphardt, P. Yang, *Nature* **2007**, *447*, 1098.
[19] L. Le Xuan, C. Zhou, A. Slablab, D. Chauvat, C. Tard, S. Perruchas, T. Gacoin, P. Villeval, J.-F. Roch, *Small* **2008**, *4*, 1332.
[20] P. Pantazis, J. Maloney, D. Wu, S. E. Fraser, *Proc. Nat. Acad. Sci.* **2010**, *107*, 14535.
[21] C.-L. Hsieh, R. Grange, Y. Pu, D. Psaltis, *Biomaterials* **2010**, *31*, 2272.
[22] B. E. Urban, P. Neogi, K. Senthilkumar, S. K. Rajpurohit, P. Jagadeeshwaran, S. Kim, Y. Fujita, A. Neogi, *IEEE J. Sel. Top. Quantum Electron.* **2012**, *18*, 1451.
[23] C. Macias-Romero, M. E. Didier, V. Zubkovs, L. Delannoy, F. Dutto, A. Radenovic, S. Roke, *Nano Lett.* **2014**, *14*, 2552.
[24] A. Rogov, Y. Mugnier, L. Bonacina, *J. Opt.* **2015**, *17*, 033001.
[25] N. Sugiyama, A. Y. Sonay, R. Tussiwand, B. E. Cohen, P. Pantazis, *Small* **2018**, *14*, 1703386.
[26] G. Malkinson, P. Mahou, É. Chaudan, T. Gacoin, A. Y. Sonay, P. Pantazis, E. Beaurepaire, W. Supatto, *ACS Photonics* **2020**, *7*, 1036.
[27] E. Bonilla, C. E. Samitt, A. F. Miranda, A. P. Hays, G. Salviati, S. DiMauro, L. M. Kunkel, E. P. Hoffman, L. P. Rowland, *Cell* **1988**, *54*, 447.
[28] K. Rouger, T. Larcher, L. Dubreil, J.-Y. Deschamps, C. Le Guiner, G. Jouvion, B. Delorme, B. Lieubeau, M. Carlus, B. Fornasari, M. Theret, P. Orlando, M. Ledevin, C. Zuber, I. Leroux, S. Deleau, L. Guigand, I. Testault, E. L. Rumeur, M. Fiszman, Y. Chérel, *Am. J. Pathol.* **2011**, *179*, 2501.
[29] F. Robriquet, A. Lardenois, C. Babarit, T. Larcher, L. Dubreil, I. Leroux, C. Zuber, M. Ledevin, J.-Y. Deschamps, Y. Fromes, Y. Cherel, L. Guevel, K. Rouger, *PLoS One* **2015**, *10*, e0123336.
[30] J. Lorant, C. Saury, C. Schleder, F. Robriquet, B. Lieubeau, E. Négroni, I. Leroux, L. Chabrand, S. Viau, C. Babarit, *Mol. Ther.* **2018**, *26*, 618.
[31] S. Schwung, A. Rogov, G. Clarke, C. Joulaud, T. Magouroux, D. Staedler, S. Passemard, T. Justel, L. Badie, C. Galez, *J. Appl. Phys.* **2014**, *116*, 114306.
[32] L. Dubreil, I. Leroux, M. Ledevin, C. Schleder, L. Lagalice, C. Lovo, R. Fleurisson, S. Passemard, V. Kilin, S. Gerber-Lemaire, M.-A. Colle, L. Bonacina, K. Rouger, *ACS Nano* **2017**, *11*, 6672.
[33] D. Staedler, S. Passemard, T. Magouroux, A. Rogov, C. M. Maguire, B. M. Mohamed, S. Schwung, D. Rytz, T. Jüstel, S. Hwu, Y. Mugnier, R. L. Dantec, Y. Volkov, *Nanomedicine: NBM* **2015**, *11*, 815.
[34] W. Denk, J. H. Strickler, W. W. Webb, *Science* **1990**, *248*, 73.
[35] P. E. Hänninen, E. Soini, S. W. Hell, *J. Microsc.* **1994**, *176*, 222.
[36] H. J. Koester, D. Baur, R. Uhl, S. W. Hell, *Biophys. J.* **1999**, *77*, 2226.
[37] K. König, H. Liang, M. W. Berns, B. J. Tromberg, *Nature* **1995**, *377*, 20.
[38] M. Y. Berezin, S. Achilefu, *Chem. Rev.* **2010**, *110*, 2641.
[39] R. Hollandi, A. Szkalisity, T. Toth, E. Tasnadi, C. Molnar, B. Mathe, I. Grexa, J. Molnar, A. Balind, M. Gorbe, M. Kovacs, E. Migh, A. Goodman, T. Balassa, K. Koos, W. Wang, J. C. Caicedo, N. Bara, F. Kovacs, L. Paavolainen, T. Danka, A. Kriston, A. E. Carpenter, K. Smith, P. Horvath, *Cell Syst.* **2020**, *10*, 453.
[40] H. Bruus, *Microscale Acoustofluidics*, The Royal Society of Chemistry, London **2014**.
[41] G. Moll, J. A. Ankrum, J. Kamhieh-Milz, K. Bieback, O. Ringdén, H.-D. Volk, S. Geissler, P. Reinke, *Trends Mol. Med.* **2019**, *25*, 149.
[42] G. Moll, I. Rasmusson-Duprez, L. von Bahr, A.-M. Connolly-Andersen, G. Elgue, L. Funke, O. A. Hamad, H. Lönnies, P. U. Magnusson, J. Sanchez, Y. Teramura, K. Nilsson-Ekdahl, O. Ringdén, O. Korsgren, B. Nilsson, K. Le Blanc, *Stem Cells* **2012**, *30*, 1565.
[43] X. Stephenne, E. Nicastro, S. Eeckhoudt, C. Hermans, O. Nyabi, C. Lombard, M. Najimi, E. Sokal, *PLoS One* **2012**, *7*, e42819.
[44] B. M. Gleeson, K. Martin, M. T. Ali, A. H. Kumar, M. G.-K. Pillai, S. P. Kumar, J. F. O'Sullivan, D. Whelan, A. Stocca, W. Khider, F. P. Barry, T. O'Brien, N. M. Caplice, *Stem Cells* **2015**, *33*, 2726.
[45] E. M. Sokal, X. Stéphenne, C. Ottolenghi, N. Jazouli, P. Clapuyt, F. Lacaille, M. Najimi, P. d. Lonlay, F. Smets, *JIMD Reports-Case and Research Reports*, vol. *13*, Springer, New york **2013**, pp. 65–72.
[46] Z. Wu, S. Zhang, L. Zhou, J. Cai, J. Tan, X. Gao, Z. Zeng, D. Li, *Transplantation Proceedings* **2017**, *49*, 1656.
[47] H. Wang, C. Strange, P. J. Nietert, J. Wang, T. L. Turnbull, C. Cloud, S. Owczarski, B. Shuford, T. Duke, G. Gilkeson, L. Luttrell, K. Hermayer, J. Fernandes, D. B. Adams, K. A. Morgan, *Stem Cells Transl. Med.* **2018**, *7*, 11.
[48] A. B. Shrirao, R. S. Schloss, Z. Fritz, M. V. Shrirao, R. Rosen, M. L. Yarmush, *Biotechnol. Bioeng.* **2021**, *118*, 4550.
[49] S. S. Moonshi, Y. Wu, H. T. Ta, *Wiley Interdiscip. Rev.: Nanomed. Nanobiotechnol.* **2022**, *14*, e1760.
[50] S. James, K. Neuhaus, M. Murphy, M. Leahy, *Stem. Cell Res. Ther.* **2021**, *12*, 1.
[51] M. Ma, Y. Shu, Y. Tang, H. Chen, *Nano Today* **2020**, *34*, 100897.
[52] T. T. Sibov, L. F. Pavon, L. A. Miyaki, J. B. Mamani, L. P. Nucci, L. T. Alvarim, P. H. Silveira, L. C. Marti, L. Gamarra, *Int. J. Nanomed.* **2014**, *9*, 337.

[53] C. Chapon, J. S. Jackson, E. O. Aboagye, A. H. Herlihy, W. A. Jones, K. K. Bhakoo, *Mol. Imaging Biol.* **2009**, *11*, 31.
[54] V. P. Nguyen, W. Fan, T. Zhu, W. Qian, Y. Li, B. Liu, W. Zhang, J. Henry, S. Yuan, X. Wang, Y. M. Paulus, *ACS Nano* **2021**, *15*, 13289.
[55] R. De Matos, A. Gheata, G. Campargue, J. Vuilleumier, L. Nicolle, K. Pierzchala, I. Jelescu, F. Lucarini, I. Gautschi, F. Riporto, R. Le Dantec, Y. Mugnier, A.-S. Chauvin, M. Mazzanti, D. Staedler, D. Diviani, L. Bonacina, S. Gerber-Lemaire, *ACS Appl. Nano Mater.* **2022**, *5*, 2912.
[56] A. Riches, J. G. Sharp, D. B. Thomas, S. V. Smith, *J. Physiol.* **1973**, *228*, 279.
[57] W. Sluiter, L. Oomens, A. Brand, R. Van Furth, *J. Immunol. Methods* **1984**, *73*, 221.
[58] N. Honkura, M. Richards, B. Laviña, M. Sáinz-Jaspeado, C. Betsholtz, L. Claesson-Welsh, *Nat. Commun.* **2018**, *9*, 2746.
[59] G. Meng, J. Zhong, Q. Zhang, J. S. Wong, J. Wu, K. K. Tsia, N. Ji, *Proc. Nat. Acad. Sci.* **2022**, *119*, 2117346119.
[60] A. Rannou, G. Toumaniantz, T. Larcher, I. Leroux, M. Ledevin, A. Hivonnait, C. Babarit, R. Fleurisson, L. Dubreil, S. Ménoret, I. Anegon, F. Charpentier, K. Rouger, L. Guével, *Mol Ther Meth Clin. Dev.* **2020**, *18*, 446.
[61] F. Ramos-Gomes, W. Möbius, L. Bonacina, F. Alves, M. A. Markus, *Small* **2019**, *15*, 1803776.
[62] R. Huber, M. Wojtkowski, J. G. Fujimoto, *Opt. Express* **2006**, *14*, 3225.
[63] R. Huber, D. C. Adler, J. G. Fujimoto, *Opt. Lett.* **2006**, *31*, 2975.
[64] A. Vogel, J. Noack, G. Hüttman, G. Paltauf, *Appl. Phys. B* **2005**, *81*, 1015.
[65] K. König, *Handbook of Biological Confocal Microscopy*, Springer, New York **2006**, pp. 680–689.
[66] V. Kilin, G. Campargue, I. Fureraj, S. Sakong, T. Sabri, F. Riporto, A. Vieren, Y. Mugnier, C. Mas, D. Staedler, J. M. C. Collins, L. Bonacina, A. Vogel, J. A. Capobianco, J.-P. Wolf, *ACS Nano* **2020**, *14*, 4087.
[67] R. Hollandi, Á. Diósdi, G. Hollandi, N. Moshkov, P. Horváth, *Mol. Biol. Cell* **2020**, *31*, 2179.
[68] S. Van der Walt, J. Schönberger, J. Nunez-Iglesias, F. Boulogne, J. Warner, N. Yager, E. Gouillart, T. Yu, *PeerJ* **2014**, *2*, e453.